Crystallographic Orientation Dependence of Corrosion Behavior of a Single Crystal Nickel-Based Alloy

L.N. ZHANG and O.A. OJO

Crystallographic orientation dependence of corrosion behavior of a nickel-based single crystal alloy IN738 was studied. Potentiodynamic polarization and electrochemical impedance spectroscopy show that corrosion performance of the single crystal alloy varies with crystallographic orientation. The dependence of passivation behavior on crystallographic orientation is influenced by environmental concentration. Potentiostatic polarization, scanning probe microscopy, and X-ray photoelectron spectroscopy were performed to understand the variation in passivation of different crystallographic orientations. The crystallographic orientation dependence of corrosion performance of the alloy can be explained by the difference of passive films in terms of chemical compositions, compactness, and porosity properties, as well as surface roughness.

I. INTRODUCTION

NICKEL-BASED alloys have been widely applied as hot section components in aerospace gas turbine engines due to their excellent mechanical properties and corrosion resistance at high temperatures.[1–5] In order to further enhance the high-temperature performance of nickel-based alloys, directional solidification casting is used to produce single crystal (SX) alloys. Previous investigations demonstrate that the properties of SX materials are generally known to vary significantly with crystallographic orientation. Several studies have focused on understanding high-temperature performance of SX nickel-based alloys under various service conditions.[6–12] The SX nickel-based alloys are known to exhibit higher creep properties along the [001] crystallographic direction compared to the [011] or [111] directions.[11] There is an anisotropic variation in yielding strength and deformation for SX nickel-based alloys with different orientations.[12]

However, aside from high-temperature properties, corrosion behavior under ambient conditions with different corrosion media is fundamental and equally worthwhile to investigate for practical application as well, as turbine vanes in aircraft engines may suffer from room-temperature corrosion during downtime.[13] Resistance to a corrosive environment at room temperature is another important property which can influence durability and service life of the alloy.[14–17] Nevertheless, very limited research has been conducted on corrosion behavior of SX nickel-based alloys.

It is known that alloying elements, such as nickel, chromium, and titanium are beneficial for nickel-based alloys to form very thin oxidized films on their surfaces in various aggressive environments.[18,19] This type of layer which is known as passive film, can significantly reduce the electrochemical reaction rates on the surface, and prominently improve corrosion resistance of the alloy. Previous results demonstrated that crystallographic orientation can control dissolution, passivation, and corrosion behavior of materials.[19–28] Although, a study has found that fabrication of nickel-based alloys in SX form can significantly enhance their resistance to corrosion compared to polycrystalline alloys,[18] the dependence of crystallographic orientation on passivation and corrosion behavior of the alloy has not yet been thoroughly investigated.

The objective of this research is to study crystallographic orientation dependence of corrosion behavior of a SX nickel-based alloy, IN 738. Electron backscatter diffraction (EBSD) was applied to determine crystallographic orientation of SX specimens. The corrosion behavior of SX nickel-based specimens with different crystallographic orientations was investigated in various corrosion environments by employing techniques of potentiostatic polarization, electrochemical impedance spectroscopy (EIS), X-ray photoelectron spectroscopy (XPS), and scanning probe microscopy (SPM).

L.N. ZHANG and O.A. OJO are with the Department of Mechanical Engineering, University of Manitoba, Room E2-327, 75A Chancellors Circle, Winnipeg, MB R3T 5V6, Canada. Contact e-mail: Lina.Zhang@umanitoba.ca

II. EXPERIMENTAL

A. Material

The metal alloy used in this study is a SX nickel-based alloy IN 738 with a chemical composition listed in Table I. Experimental specimens were cut from a commercial cylindrical single crystal rod. Three conveniently sectioned planes were selected as shown in Figure 1, S1 is the cross-sectional plane, and S2 and S3 were sectioned at 45 deg and 75 deg to the cross-sectional plane, respectively. Specimens were ground by wet silicon carbide paper with decreasing grit size (180, 600, 800, 1200), then mechanical polished to 1 μm with alumina. The final stage of sample preparation was followed by polishing the surface with 0.04 μm colloidal silica to obtain a mirror-like and strain-free surface for orientation measurement.

The specimens for electrochemical corrosion tests were embedded in a bakelite mount leaving an exposed working area of 1 cm^2. The sample preparation of corrosion experiments was mechanical polished to 1 μm, then followed by degreasing with an acetone ultrasonic bath for 5 minutes, and rinsed in distilled water and dried at 30 °C.

B. Methods

The crystallographic orientations of the samples were determined using a scanning electron microscope (SEM) equipped with an Oxford Instrument NordlysNano EBSD detector. The generated raw data were analyzed by employing the Oxford Instrument Channel 5 post-processing software. The surface orientations of the three samples were described by the Euler angles (φ_1, Φ, φ_2) and Miller indices (hkl) as presented in Table II.

Electrochemical corrosion tests were performed in a conventional three-electrode electrochemical cell arrangement, using a saturated calomel electrode (SCE) as the reference electrode and carbon rods as the counter electrodes. A luggin capillary was used to control placement of the reference electrode relative to the working electrode. Both data acquisition and analysis were carried out by applying the Princeton Applied Research Potentiostat with VersaStudio software. The experiments were carried out in different solutions: 0.5 M hydrochloric acid (HCl), 0.5 M nitric acid (HNO$_3$), and sulfuric acid (H$_2$SO$_4$) at three different concentrations of 0.5 M, 2 M, and 5 M. To avoid air-formed oxides, the freshly polished samples were immediately assembled and transferred into the corrosion cell kit filled with the aforementioned electrolytes. Prior to all electrochemical measurements, open circuit potential measurements were carried out for 1 hour to achieve stable corrosion potentials. All potential values were obtained with reference to the SCE.

Three different electrochemical techniques were employed in this study: potentiodynamic polarization, potentiostatic polarization, and electrochemical impedance spectroscopy (EIS). Potentiodynamic polarization tests were performed at a scan rate of 1 mV/s. The potentiodynamic polarization curves were used to characterize the corrosion current density (i_{corr}), critical current density (i_{crit}), passive current density (i_{pass}), corrosion potential (E_{corr}), and potential range of passivation (ΔE_{pass}). Potentiostatic polarization experiments were carried out at the potential of 0.5 V, which is well within the passive potential range of each sample. The variation of current density with time was measured at the potential of 0.5 V for 1 hour to obtain information about the formation of passivation films. EIS measurements were performed on the passive films which was formed at the potential of 0.5 V for 1 hour. The potential was the open circuit potential, and the frequency was scanned from 10^4 Hz down to 10^{-2} Hz at an AC potential amplitude of 10 mV. ZSimpWin software was employed to analyze EIS data. All electrochemical experiments were conducted in the same volume of corrosive solution (500 mL) at room temperature (around 25 °C) and repeated at least three times to ensure reproducibility.

The samples passivated after potentiostatic polarization at 0.5 V for 1 hour were carefully cut to an approximate thickness of 2 mm and cleaned with ethyl alcohol for X-ray photoelectron spectroscopy (XPS) and scanning probe microscope (SPM) analyses. XPS analysis was performed on a Kratos Axis Ultra DLD X-ray Photoelectron Spectrometer with an Al K$_\alpha$ (1486.6 eV) monochromatic source under a pressure below 10^{-8} Torr. The survey scan was executed between 0 and 1200 eV. The C 1s peak with a binding energy of 285 eV was used as a reference to correct the surface charging shifts. High-resolution scans were recorded for Cr 2p, Ti 2p, and Ni 2p. Peaks were fitted using Gaussian–Lorentzian function after background subtraction with CasaXPS software. Quantification of the XPS intensities for Cr, Ti, and Ni was carried out. The surface roughness of the passive films was evaluated using a TI 750 UBI SPM. The probe is Berkovich tip with a radius of 100 nm.

III. RESULTS AND DISCUSSION

A. Study of Corrosion Behavior in Different Corrosive Environments

Previous studies found that the influence of crystallographic orientation on corrosion behavior was affected by the environment.[29,30] In this study, the dependence of crystallographic orientation on corrosion

Table I. Chemical Composition of Experimental Material (Weight Percent)

Element	C	Cr	Mo	W	Al	Ti	Co	Nb	Zr	B	Ni
IN738	0.17	16.0	1.75	2.60	3.40	3.40	8.50	0.90	0.05	0.01	bal

behavior was investigated under different environments. The potentiodynamic polarization plots of three SX samples S1, S2, and S3 in different corrosive environments containing 0.5 M H_2SO_4, HNO_3, and HCl are shown in Figure 2. The results show that all the samples exhibit active–passive–transpassive behavior in both H_2SO_4 and HNO_3 solutions (Figures 2(a) and (b)). The evaluations of corrosion characteristics of the samples in H_2SO_4 and HNO_3 environments are presented in Tables III and IV, where i_{corr}, i_{crit}, and i_{pass} represent the corrosion current density, critical current density (maximum current density of active–passive transition), and passive current density, respectively. E_{corr} and ΔE_{pass} are the corrosion potential and potential range of passivation, respectively. In the H_2SO_4 environment, the corrosion current density values of i_{corr}
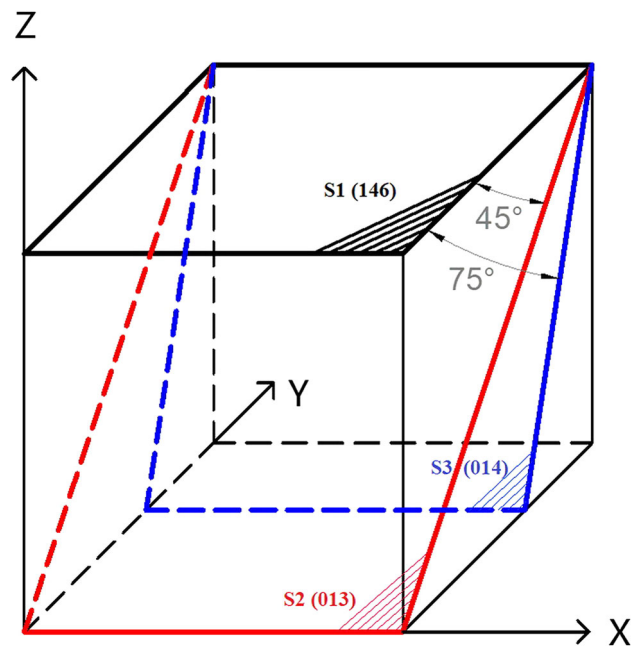
of the three SX samples are slightly different, and the i_{corr} of S1 is a little bit smaller compared to those of S2 and S3. However, there is a significant difference at the passive region where the i_{crit} and i_{pass} values of SX sample S1 are one order of magnitude higher than that of SX samples S2 and S3. The passivation potential range ΔE_{pass} shrinks in the order of S3 > S2 > S1. In the HNO_3 environment, the SX sample S1 shows the highest value of i_{corr}, i_{crit}, and i_{pass} among the three SX samples, while sample S3 presents the best corrosion resistance at both active and passive regions. The passivation behavior of all three samples is atypical in the HCl solution compared to those in H_2SO_4 and HNO_3 solutions (Figure 2(c)). This is due to the fact that Cl^- ions have strong tendencies to adhere to the surface of metallic materials and penetrate into the bulk alloy through the defects of the surface passive film, which in turn damage the protective capability of the passive layer.[31–33] It is well known that a key mechanism for both nickel-based alloys and stainless steels exhibiting good corrosion resistance under some aggressive environments is the formation of passive films.[34–39] In all of these different corrosive solutions, the SX sample S3 exhibits the lowest anodic current density values of i_{pass} throughout the entire potential range 0.0 to 1.0 V within which the samples normally exhibit passivation behavior. The sample S3 is followed by S2, and then S1, in terms of the highest anodic current density values at the passive region. It is demonstrated that in different corrosive environments, SX sample S3 shows the best passivation behavior, while that of sample S1 is the least. Hence, the results suggest that the corrosion performance of the SX alloy IN 738 is significantly dependent on crystallographic orientation.

To further study the variation in corrosion performance of the SX alloy with different crystallographic orientations, the effect of increase in H_2SO_4 concentration on corrosion behavior of SX samples S1, S2, and S3 was investigated. In addition to the potentiodynamic polarization results in 0.5 M shown in Figure 2(a), the results of the tests performed in 2 M and 5 M solutions are presented in Figures 3(a) and (b), respectively. The increase in concentration from 0.5 to 5 M produced a

Fig. 1—Preparation of specimen surfaces of three different crystallographic orientations.

Table II. Euler Angles and Crystallographic Indices of Different Single Crystal Planes

Single Crystal Plane	φ_1	Φ	φ_2	(hkl)
S1	348	32	14	(146)
S2	165	21	12	(013)
S3	158	16	15	(014)

Table III. Corrosion Characteristics of Different Single Crystal Planes in 0.5 M H_2SO_4

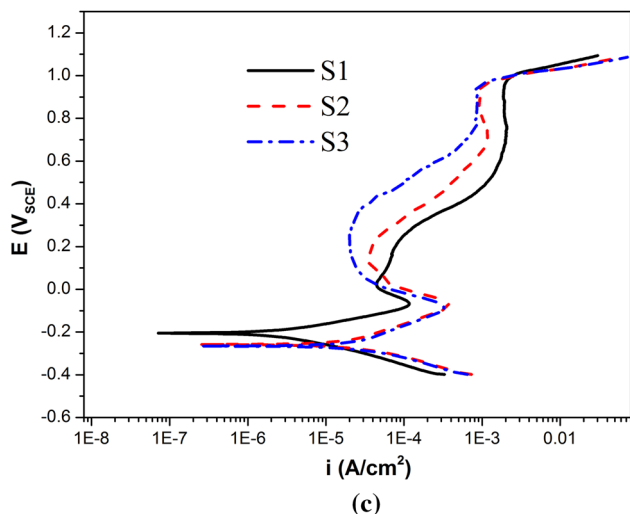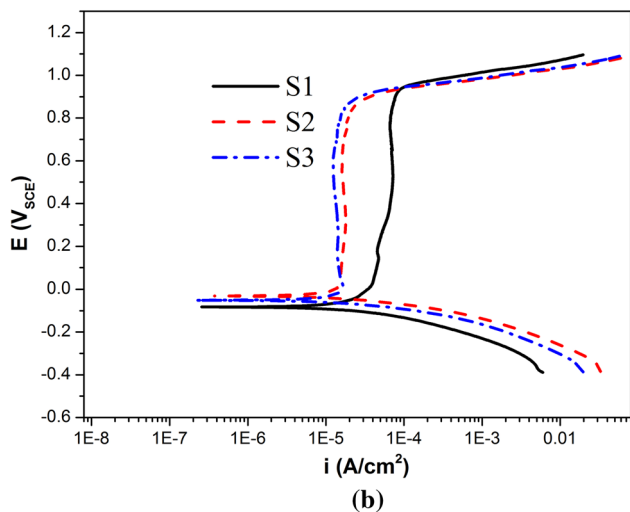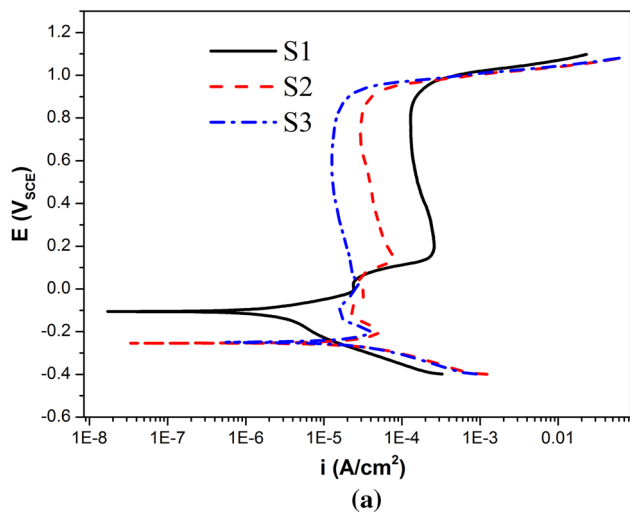| Single Crystal Plane	E_{corr} (mV)	i_{corr} ($\mu A/cm^2$)	i_{crit} ($\mu A/m^2$)	i_{pass} ($\mu A/cm^2$)	Potential Range of Passivation ΔE_{pass} (mV)
S1	− 96.9 ± 12.6	2.6 ± 0.6	451.8 ± 15.2	203.9 ± 12.6	557.5 ± 26.2
S2	− 237.2 ± 14.4	5.2 ± 0.9	55.1 ± 6.5	21.2 ± 4.7	623.6 ± 10.5
S3	− 256.6 ± 25.2	6.0 ± 0.8	26.5 ± 9.8	10.9 ± 1.9	845.0 ± 22.6

Fig. 2—Potentiodynamic polarization plots of different single crystal planes in different corrosive solutions (a) 0.5 M H_2SO_4, (b) 0.5 M HNO_3, (c) 0.5 M HCl.

significant increase in the passive anodic current density value (i_{pass}) in SX sample S3. The increase of i_{pass} also occurred in SX sample S2 but to a lesser extent, while there is a negligible change in i_{pass} of SX sample S1. The results show that the passivation behavior of sample S3 is quite sensitive to the change in concentration, while sample S2 exhibits a passivation performance that varies with concentration to a lesser extent. The passivation behavior of sample S1 in the corrosive environment is nearly insensitive to the change in concentration. The pattern of change in passivation with concentration is exhibited by the three samples. This leads us to believe that the crystallographic orientation dependence of passivation behavior of the SX alloy becomes more pronounced as the sulfuric acid concentration decreases.

B. Study of Passivation Using Electrochemical Impedance Spectroscopy (EIS)

Based upon the analysis of corrosion behavior in different corrosive environments, SX samples can form a passive layer under certain aggressive environments, which is beneficial for the corrosion behavior of the alloy. To further evaluate the influence of crystallographic orientation on corrosion behavior of SX alloy IN738, EIS measurements were performed on samples with different orientations after passivation at 0.5 V for 1 hour in 0.5 M H_2SO_4. Figure 4 shows the EIS spectra of SX specimens S1, S2, and S3 after passivation. The Nyquist plots in Figure 4(a) have similar shapes with only one capacitive loop in the entire frequency range, but diameters of unfinished semicircle arc of the three samples with different crystallographic orientations are different. This suggests that corrosion-resistant behavior depends on crystallographic orientation. The Bode plots in Figure 4(b) show the different impedances at low frequencies (at 10^{-2} Hz, log|Z| increases in the order of S1 < S2 < S3), indicating the difference in corrosion performance. The relationship between log|Z| and frequency is similar and close to linear when the frequency is over 1 Hz. The Bode plots of the phase angle in Figure 4(c) indicate that only one time constant exists in the analyzed system. The variations of the phase angle of S2 and S3 are comparable in the entire frequency range, and the values of the phase angle of S2 and S3 are higher than that of S1. Figure 5 shows the electrical equivalent circuit, which is used to evaluate the EIS spectra. In the circuit model, R_s is the solution resistance, R_{ct} is the charge transfer resistance, the constant phase element (CPE) is a capacitive description of the electrical double layer at the passive film/metal interface. The relationship between the impedance of CPE (Z_{CPE}) and the capacitance is given by the following Eq. [1][30,36,40]

$$Z_{CPE} = Q_0^{-1}(j\omega)^{-n},$$ [1]

where Q_0 is the magnitude of CPE, $j^2 = -1$ is an imaginary number, ω is the angular frequency, and n is an exponential factor. When $n = 0$, the CPE resembles a resistor, when $n = 1$, the CPE acts as a pure capacitor, and n ranges from 0 to 1 under normal experimental conditions. As can be seen in Figure 4, there is good agreement between the simulation results and the experimental data. The calculated impedance

Table IV. Corrosion Characteristics of Different Single Crystal Planes in 0.5 M HNO₃

Single Crystal Plane	E_{corr} (mV)	i_{corr} ($\mu A/cm^2$)	i_{crit} ($\mu A/cm^2$)	i_{pass} ($\mu A/cm^2$)	Potential Range of Passivation ΔE_{pass} (mV)
S1	-82.3 ± 7.8	14.0 ± 2.4	85.5 ± 9.5	78.5 ± 9.4	602.0 ± 80.5
S2	-32.1 ± 8.0	5.0 ± 0.9	17.4 ± 4.6	15.4 ± 2.5	800.0 ± 55.8
S3	-44.0 ± 10.6	2.5 ± 0.4	14.5 ± 0.8	10.6 ± 1.2	782.5 ± 49.5
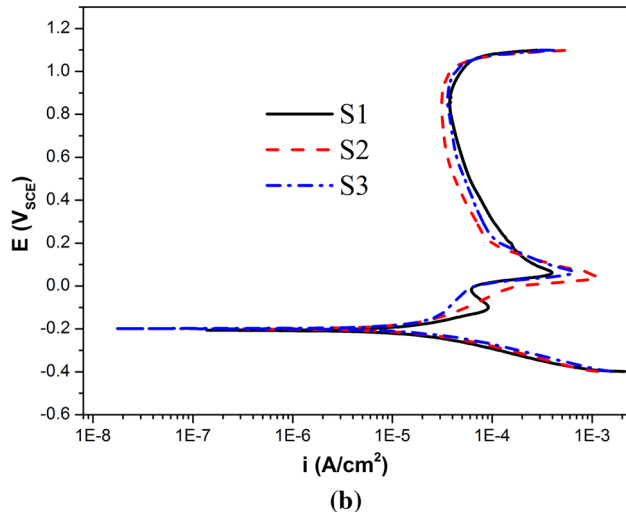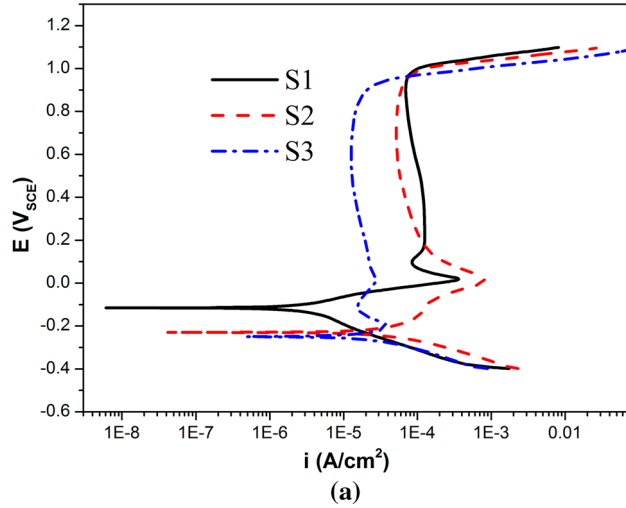
Fig. 3—Potentiodynamic polarization plots of different single crystal planes in H_2SO_4 with different concentrations (a) 2 M, (b) 5 M.

parameters of the three samples are listed in Table V. The results show that the charge transfer resistance R_{ct} increases in the order of S1 < S2 < S3, and the capacitance value decreases in the order of S1 > S2 > S3. The difference in the charge transfer process at the electrolyte/electrode interface is significantly related to the properties of the surface passive films.[18] The capacitive behavior may be related to the electrical double layer at the solution/metal interface, the passive film/metal surface, or both.[41] It is suggested that the passive film

formed on S1 has the lowest corrosion resistance, followed by the other two samples S2 and S3. Based on the EIS results, it can be concluded that the corrosion resistance of the passive surface formed in 0.5 M H_2SO_4 depends on the crystallographic orientation.

It is found that the passive film protective ability depends upon chemical composition, structure, thickness, and electronic properties.[42–45] The passive films formed on alloy surfaces are very thin, approximately just few nanometer. Therefore, it is difficult to measure the thickness or observe the morphology using traditional optical microscopy and scanning electron microscopes. In order to investigate the properties of the passive films formed on S1, S2, and S3, potentiostatic polarization, XPS, and SPM were performed and the results are discussed in the following.

C. Characterization of Passive Films by Using Potentiostatic Polarization, Scanning Probe Microscopy (SPM), and XPS

A passive film is normally formed on the surface of a metal in a corrosive environment within the passivation potential range. Generally, a compact passive film structure with low porosity produces a higher corrosion resistance compared to a less compact passive film with high porosity. This aids ionic diffusion and facilitates corrosion.[18] According to EIS results, the variations in the corrosion resistance values of the surface passive films formed on the three samples with different orientations indicate that the structures of the passive films, in term of compactness, may be different. The variation of current density with time at a fixed potential, within the passivation potential range, can be appropriately measured using potentiostatic polarization. In this study, the change in current density with time for the three samples, S1, S2, and S3 was measured by potentiostatic polarization at 0.5 V for 1 hour under 0.5 M H_2SO_4 solution. The relationship between the current density and time can be expressed by the Eq. [2].[46]

$$i = 10^{-(a+b\log t)}, \qquad [2]$$

where i is the current density, t is the time, a and b are constants. In a double-logarithmic plot of Eq. [2], b is the plot's slope.

The slope $b = -1.0$, it indicates a field-controlled surface passive film formation process. This process produces a well compact passive film structure with minimal porosity, which exhibits corrosion protection
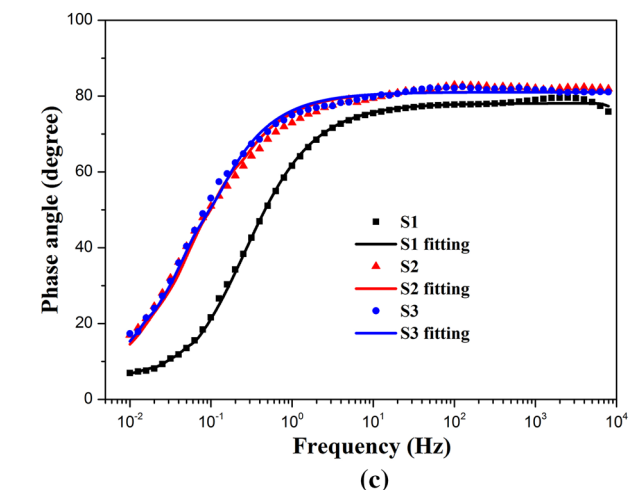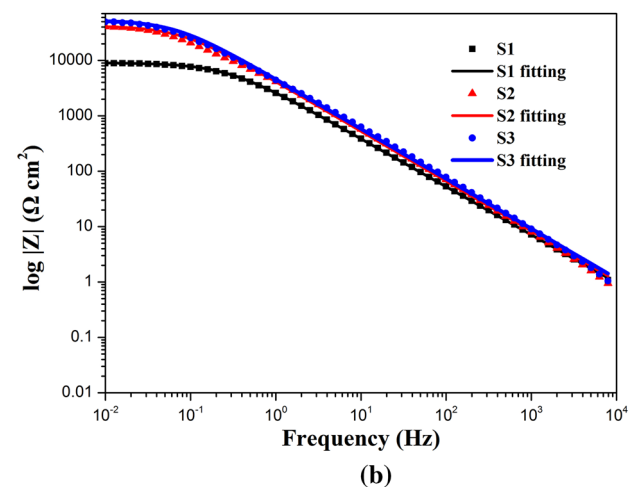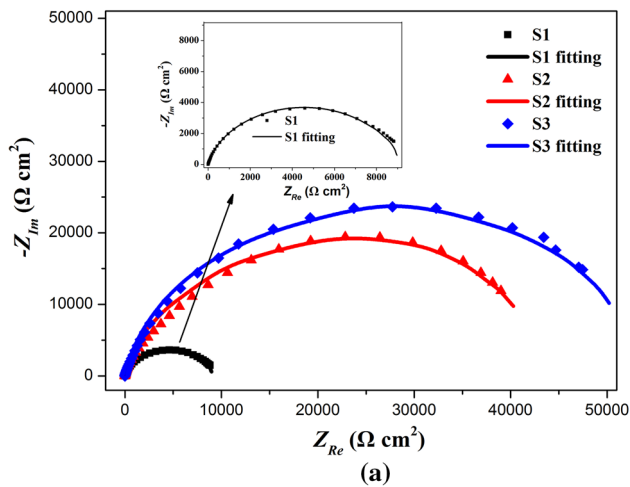
(a)

(b)

(c)

Fig. 4—EIS spectra of different single crystal planes after passivation at 0.5 V for 1 h in 0.5 M H_2SO_4 (a) Nyquist plots, (b) Bode plots—impedance, (c) Bode plots—phase angle.

properties. The value of $b = -0.5$ indicates a diffusion-controlled surface passive film formation, and growth. This process produces a porous structure, which has weak corrosion protective capabilities.[46,47] The double-logarithmic plots of the data obtained from
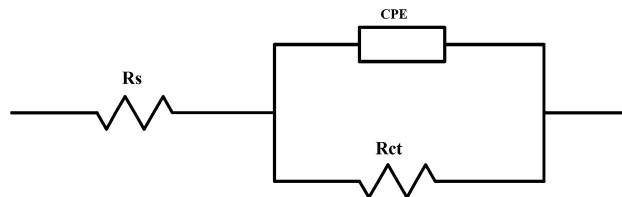

Fig. 5—Equivalent circuit modeling the electrode system.

potentiostatic polarization tests of the three samples are shown in Figure 6. The slope of S1 is close to -0.5, while the slopes for S2 and S3 are close to -1.0. These results indicate that the passive films formed on S2 and S3 are compact, while the film formed on S1 is less compact and more porous. The results also suggest that the compactness of the passive film on S3 may be slightly higher than that of S2.

The surface roughness values (mean roughness R_a) of the three samples, as determined by scanning probe microscopy, are shown in Figure 7. The surface roughness value of the passive film formed on sample S1 is the largest followed by the one formed on S2 and then S3. The surface roughness value of S1 is nearly twice as much as that of S3. In general, the compactness of a passive film can influence its surface roughness, and an increase in the porosity of a surface film can cause an increase in its surface roughness value.[48] Therefore, the results of roughness measurement corroborate the results of double-logarithmic plots of potentiostatic polarization data which indicate that the passive films formed on S3 and S2 are less porous than that formed on S1.

For investigating the differences of passive films in terms of chemical compositions, XPS analysis was performed. Survey scans were performed to identify all detectable elements in the passive films formed after being polarized at 0.5 V for 1 hour under 0.5 M H_2SO_4. The XPS survey spectra of three different oriented planes are depicted in Figure 8. High-resolution XPS scans show that Ni2p, Cr2p, and Ti2p peaks are made up of both metallic and oxidized states, but Mo, W, and Co peaks consist of only metallic components. The spectra deconvolutions of the passive film primary compounds of Ti, Cr, and Ni are performed based upon the corresponding binding energies listed in Table VI. The XPS spectra of Ni2p, Cr2p, and Ti2p were fitted and identified according to the NIST database as shown in Figures 9, 10, 11. The chemical compositions of passive films were estimated by considering the ratio of oxidized to unoxidized metals from the high-resolution spectra for each peak.[19] The passive film compositions formed on the three specimens are listed in Table VII. It is obvious that Cr_2O_3 is the dominant corrosion product of the passive films formed on these three samples. Previous studies showed that structures of both Cr_2O_3 and TiO_2 are generally compact with low porosity.[19,49–51] In contrast, $Ni(OH)_2$ exhibits a more porous structure compared to Cr_2O_3 and TiO_2.[18,52] Hence, a parameter to represent the protective capability (R_{PC}) of the passive films formed

Table V. Equivalent Circuit Parameters of EIS Results of Different Single Crystal Planes After Passivation at 0.5 V for 1 h under 0.5 M H₂SO₄

Single Crystal Plane	R_s (Ω cm²)	CEP (F cm⁻² s^(n−1))	n	R_{ct} (Ω cm²)
S1	1.18	7.084E−5	0.87	9108
S2	1.29	4.549E−5	0.91	42230
S3	1.42	4.125E−5	0.90	53190
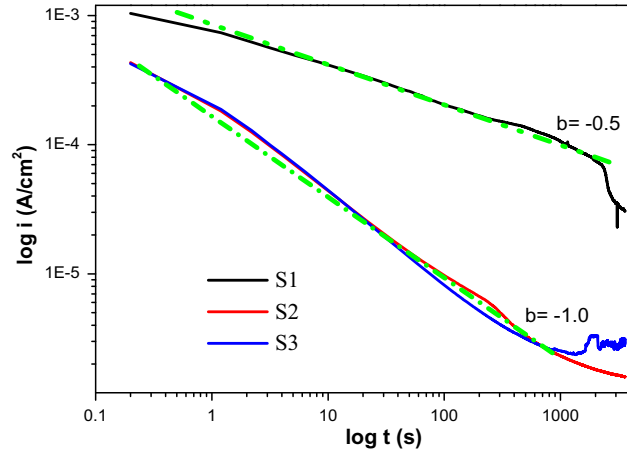
Fig. 6—Double-logarithmic plots of current–time for different single crystal planes as obtained by potentiostatic polarization tests (at 0.5 V for 1 h under 0.5 M H₂SO₄).
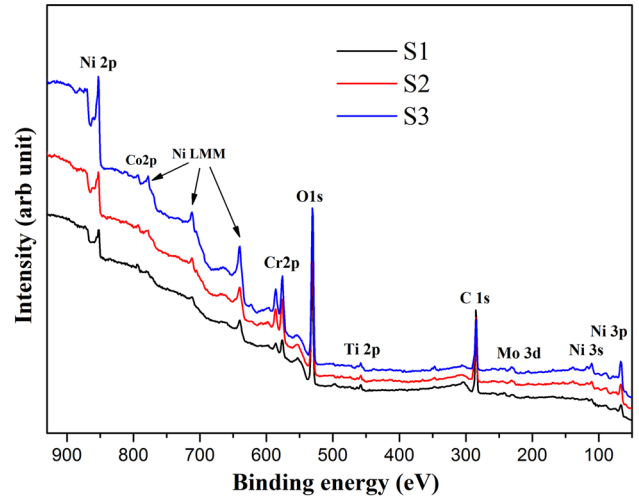

Fig. 8—Wide XPS survey spectra of passive films of different single crystal planes after passivation at 0.5 V for 1 h under 0.5 M H₂SO₄.

Fig. 7—The roughness value (R_a) of different single crystal planes after passivation at 0.5 V for 1 h under 0.5 M H₂SO₄.

Table VI. Binding Energies of the Primary Passive Film Compounds Formed on Single Crystal Planes from XPS Spectra Deconvolution

Element	Peak	Species/Binding Energy (eV)
Ti	2p₃/₂	TiO₂/458.5;Ti(metal)/454.3
	2p₁/₂	TiO₂/464.7;Ti(metal)/460.1
Cr	2p₃/₂	Cr₂O₃/576.6;Cr(metal)/573.9
	2p₁/₂	Cr₂O₃/586.4;Cr(metal)/583.5
Ni	2p₃/₂	Ni(OH)₂/855.9;Ni(metal)/852.6
	2p₁/₂	Ni(OH)₂/873.7;Ni(metal)/870.0

on samples S1, S2, and S3, based on their structural compactness that influences corrosion resistance can be given by Eq. [3]

$$R_{PC} = \frac{Cr_2O_3 + TiO_2}{Ni(OH)_2} \qquad [3]$$

The computed values of R_{PC} for the three samples are presented in Table VIII. The results show that the total quantity of Cr₂O₃ and TiO₂ relative to Ni(OH)₂ is the highest on S3 followed by S2 and then S1. This could explain the variation in the degree of compactness of the passive films formed on the three specimens. An increase in the formation of Cr₂O₃ and TiO₂ relative to Ni(OH)₂ would enhance the compactness of the surface passive film, which will in effect increase its electrical resistance and aid the corrosion resistance of the alloy. Accordingly, the higher structural compactness of the passive films and the concomitant higher corrosion resistance, on samples S3 and S2 compared to S1, seem to have been caused by higher amounts of Cr₂O₃ and TiO₂ relative to Ni(OH)₂ formed on S3 and S2 compared to S1. The difference in the value of R_{PC} of S1, S2, and S3 indicates that the formation of the Cr₂O₃, TiO₂, and
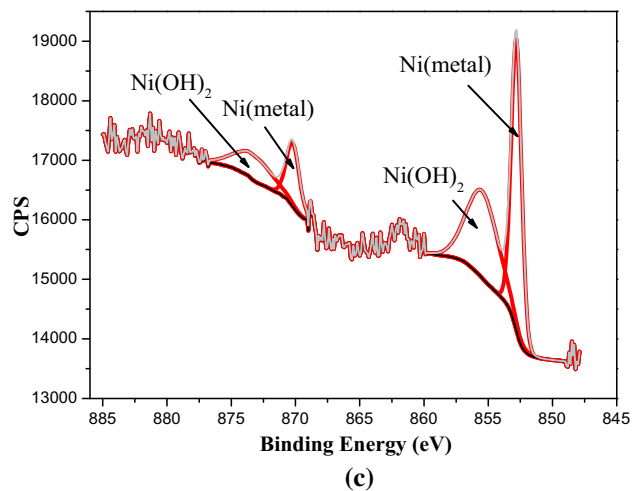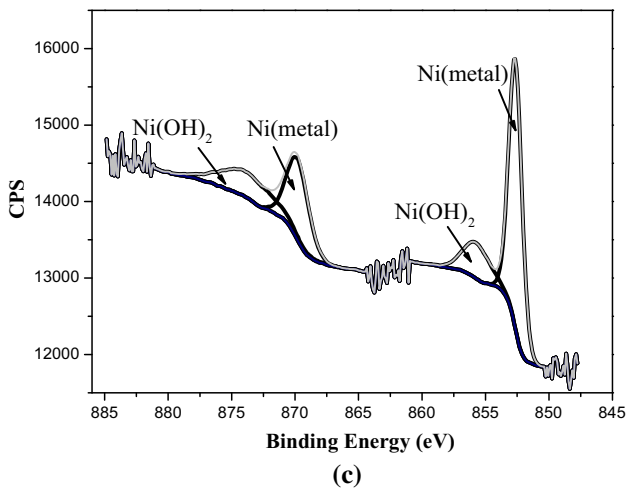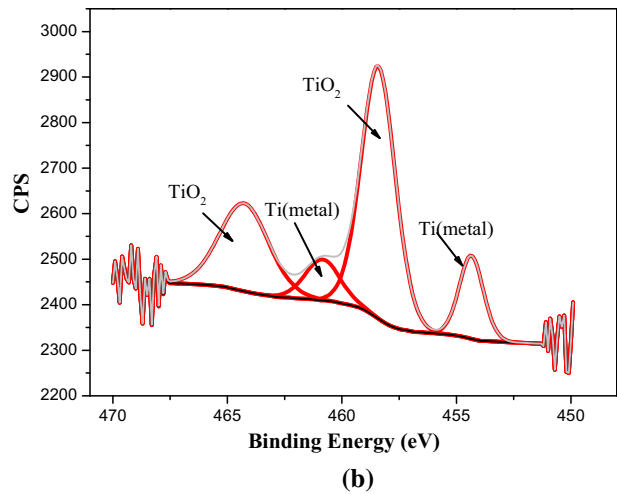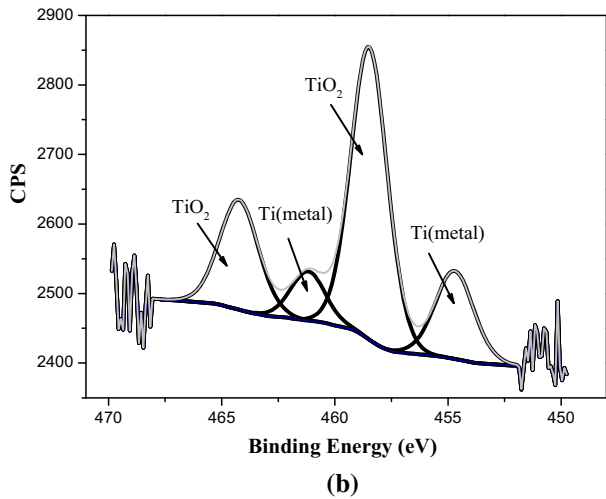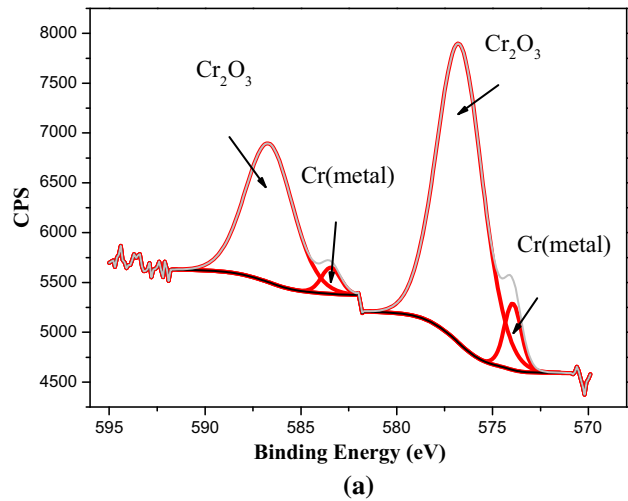
Fig. 9—High-resolution XPS spectra of passive film formed on S1 after passivation at 0.5 V for 1 h under 0.5 M H$_2$SO$_4$ (*a*) Cr2p, (*b*) Ti2p, (*c*) Ni2p.

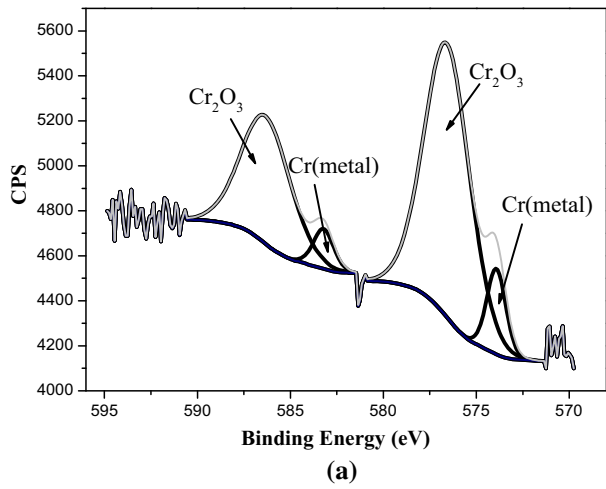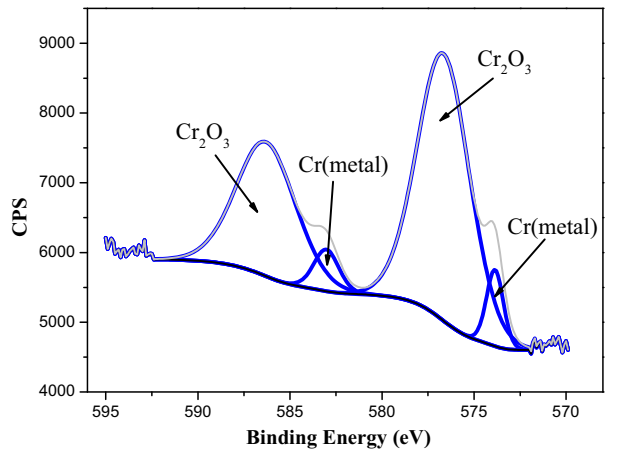Fig. 10—High-resolution XPS spectra of passive film formed on S2 after passivation at 0.5 V for 1 h under 0.5 M H$_2$SO$_4$ (*a*) Cr2p, (*b*) Ti2p, (*c*) Ni2p.

Ni(OH)$_2$, on the surface passive films is influenced by crystallographic orientation. A previous work in which crystallographic orientation alters the nature of surface passive film formed by corrosion reaction on a SX

copper material has been also reported in the literature.[53] Therefore, this study shows that crystallographic orientation dependence of corrosion behavior of the SX alloy IN 738, may be attributable to the
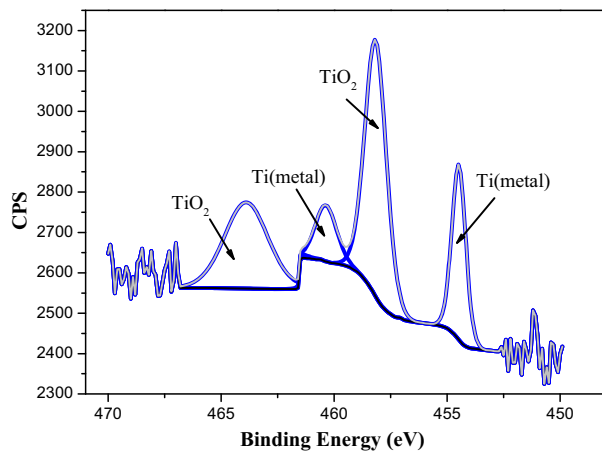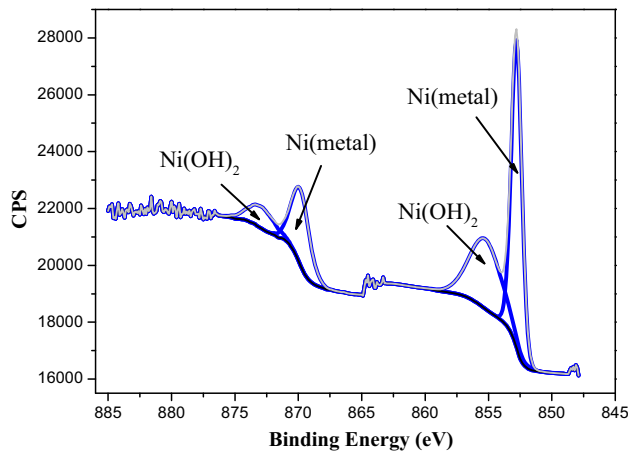
Fig. 11—High-resolution XPS spectra of passive film formed on S3 after passivation at 0.5 V for 1 h under 0.5 M H_2SO_4 (*a*) Cr2p, (*b*) Ti2p, (*c*) Ni2p.

Table VII. Passive Film Compositions from XPS Analysis After Passivation at 0.5 V for 1 h Under 0.5 M H_2SO_4 (Atomic Percent)

Single Crystal Plane	Cr_2O_3	TiO_2	$Ni(OH)_2$
S1	64.59	17.78	17.63
S2	72.15	10.76	17.09
S3	76.95	7.27	15.78

Table VIII. Protective Capability (R_{PC}) of Passive Films on Different Single Crystal Planes After Passivation at 0.5 V for 1 h Under 0.5 M H_2SO_4

Single Crystal Plane	S1	S2	S3
Protective capability (R_{PC})	4.66	4.85	5.34

IV. CONCLUSIONS

1. Potentiodynamic polarization test shows that the corrosion behavior of the SX alloy IN 738 varies with crystallographic orientation. This is corroborated by the results of EIS data analysis.
2. SX alloy exhibits passivation under an aggressive environment of sulfuric acid. Increase in the concentration of sulfuric acid produced significant changes in the passivation behavior of the alloy along certain crystallographic orientations while smaller and negligible changes occurred along other orientations. This behavior results in a situation where the orientation dependence of corrosion performance of the alloy becomes increasingly pronounced as the solution concentration reduces.
3. Analysis of potentiostatic polarization results as well as scanning probe microscopy shows that the variation in the corrosion resistance of the alloy with different crystallographic orientations is attributable to the difference in structure, in terms of the compactness of the passive films that are formed on the SX material during corrosion. The higher degree of compactness of surface passive film exhibits the higher resistance to corrosion.
4. Chemical composition analysis by XPS reveals that the relative proportion of Cr_2O_3, TiO_2, and $Ni(OH)_2$ varies with the crystallographic orientations. The protective capability of the passive films against corrosion can be expressed by a parameter ratio, $R_{PC} = (Cr_2O_3 + TiO_2)/Ni(OH)_2$.
5. The crystallographic orientation dependence of corrosion behavior of the SX alloy IN 738 is caused by variation in the values of R_{PC} produced along different orientations.

variation in the proportion of surface passive film constituents, Cr_2O_3, TiO_2, and $Ni(OH)_2$, that are formed along the different crystallographic orientations of the material.

REFERENCES

1. J.H. Tundermann: *Acta Metall. Sin*., 1996, vol. 9, pp. 423–32.
2. M.B. Henderson, D. Arrell, M. Heobel, R. Larsson, and G. Marchant: *Sci. Technol. Weld. Join.*, 2004, vol. 9, pp. 13–21.
3. P. Lortrakul, R.W. Trice, K.P. Trumble, and M.A. Dayananda: *Corros. Sci.*, 2014, vol. 80, pp. 408–15.
4. A. Pineau and S.D. Antolovich: *Eng. Fail. Anal.*, 2009, vol. 16, pp. 2668–97.
5. L.N. Zhang, P. Wang, J.X. Dong, and M.C. Zhang: *Mater. Sci. Eng. A*, 2013, vol. 587, pp. 168–78.
6. C.J. Pierce, A.N. Palazotto, and A.H. Rosenberger: *Mater. Sci. Eng. A*, 2010, vol. 527, pp. 7484–89.
7. N.R. Sun, L.T. Zhang, Z.G. Li, and A.D. Shan: *Mater. Sci. Eng. A*, 2014, vol. 606, pp. 417–25.
8. G.R. Leverant, B.H. Kera, and J.M. Oblak: *Metall. Trans.*, 1973, vol. 4, pp. 355–62.
9. T.P. Gabb, J. Gayda, and R.V. Miner: *Metall. Trans. A*, 1986, vol. 17, pp. 497–505.
10. X.G. Wang, J.L. Liu, T. Jin, and X.F. Sun: *Mater. Sci. Eng. A*, 2014, vol. 598, pp. 154–61.
11. V. Sass, U. Glatzel, and M. Feller-Kniepmeier: *Acta Mater.*, 1996, vol. 44, pp. 1967–77.
12. L.N. Wang, Y. Liu, J.J. Yu, Y. Xu, X.F. Sun, H.R. Guan, and Z.Q. Hu: *Mater. Sci. Eng. A*, 2009, vol. 505, pp. 144–50.
13. L.N. Ma and Z. Zhang: *Mater. Corros.*, 2015, vol. 66, pp. 803–10.
14. T. Bellezze, G. Roventi, and R. Fratesi: *Electrochim. Acta*, 2004, vol. 49, pp. 3005–14.
15. J.M. Le Canut, S. Maximovitch, and F. Dalard: *J. Nucl. Mater.*, 2004, vol. 334, pp. 13–27.
16. Y.Y. Chen, L.B. Chou, and H.C. Shih: *Mater. Sci. Eng. A*, 2005, vol. 396, pp. 129–37.
17. K.V. Rybalka, L.A. Beketaeva, and A.D. Davydov: *Corros. Sci.*, 2012, vol. 54, pp. 161–66.
18. L. Liu, Y. Li, and F.H. Wang: *Electrochim. Acta*, 2007, vol. 52, pp. 7193–202.
19. A.C. Lloyd, J.J. Noël, S. Mc, and D.W.Shoesmith. Intyre: *Electrochim. Acta*, 2004, vol. 49, pp. 3015–27.
20. A. Sato, K. Kon, S. Tsujikawa, and Y. Hisamatsu: *Mater. Trans.*, 1996, vol. 37, pp. 729–32.
21. K.A. Lill, A.W. Hassel, G. Frommeyer, and M. Stratmann: *Electrochim. Acta*, 2005, vol. 51, pp. 978–83.
22. A. Schreiber, J.W. Schultze, M.M. Lohregel, F. Káramán, and E. Kálmán: *Electrochim. Acta*, 2006, vol. 51, pp. 2625–30.
23. K. Fushimi, T. Okawa, K. Azumi, and M. Seo: *J. Electrochem. Soc.*, 2000, vol. 147, pp. 524–29.
24. E. Martinez-Lombardia, Y. Gonzalez-Garcia, L. Lapeire, I. De Graeve, and K. Verbeken: *Electrochim. Acta*, 2014, vol. 116, pp. 89–96.
25. U. Konig and B. Dacepon: *Electrochim. Acta*, 2001, vol. 47, pp. 149–60.
26. M. Liu, D. Qiu, M.C. Zhao, G.L. Song, and A. Atrens: *Scripta Mater.*, 2008, vol. 58, pp. 421–24.
27. A. Shahryari, J.A. Szpunar, and S. Omanovic: *Corros. Sci.*, 2009, vol. 51, pp. 677–82.
28. A.C. Schuh, K. Anderson, and C. Orme: *Surf. Sci.*, 2003, vol. 544, pp. 183–92.
29. N. Gaillard, D. Mariolle, F. Bertin, M. Gros-Jean, M. Proust, A. Bsiesy, A. Bajolet, S. Chhun, and M. Djebbouri: *Microelectron. Eng.*, 2006, vol. 83, pp. 2169–74.
30. J.J. Gray, B.S.E.I. Dasher, and C.A. Orme: *Surf. Sci.*, 2006, vol. 600, pp. 2488–94.
31. M.V. Cardoso, S.T. Amaral, and E.M.A. Martine: *Corros. Sci.*, 2008, vol. 50, pp. 2429–36.
32. A. Bouzoubaa, B. Diawara, V. Maurice, C. Minot, and P. Marcus: *Corros. Sci.*, 2009, vol. 51, pp. 2174–82.
33. A. Dhanapal, S.R. Boopathy, and V. Balasubramanian: *J Alloy. Compd.*, 2012, vol. 523, pp. 49–60.
34. N.E. Hakiki: *Corros. Sci.*, 2011, vol. 53, pp. 2688–99.
35. L.Q. Guo, M.C. Lin, L.J. Qiao, and A.A. Volinsky: *Corros. Sci.*, 2014, vol. 78, pp. 55–62.
36. F. Mohammadi, T. Nickchi, M.M. Attar, and A. Alfantazi: *Electrochim. Acta*, 2011, vol. 56, pp. 8727–33.
37. B. Peng, B.T. Lu, J.L. Luo, Y.C. Lu, and H.Y. Ma: *J. Nucl. Mater.*, 2008, vol. 378, pp. 333–40.
38. W. Fredriksson, S. Malmgren, T. Gustafsson, M. Gorgoi, and K. Edström: *Appl. Surf. Sci.*, 2012, vol. 258, pp. 5790–97.
39. M.D.C. Belo, N.E. Hakiki, and M.G.S. Ferreira: *Electrochim. Acta*, 1999, vol. 44, pp. 2473–81.
40. D. Wallinder, J. Pan, C. Leygraf, and A. Delblanc-Bauer: *Corros. Sci.*, 1998, vol. 41, pp. 275–89.
41. Z. Xiao, Z. Li, A.Y. Zhu, Y.Y. Zhao, J.L. Chen, and Y.T. Zhu: *Corros. Sci.*, 2013, vol. 76, pp. 42–51.
42. J.W. Schultze and M.M. Lohreengel: *Electrochim. Acta*, 2000, vol. 45, pp. 2499–2513.
43. U. Trdan and J. Grum: *Corros. Sci.*, 2012, vol. 59, pp. 324–33.
44. G.L. Song and Z.Q. Xu: *Corros. Sci.*, 2012, vol. 63, pp. 100–12.
45. G. Baril and N. Pébère: *Corros. Sci.*, 2001, vol. 43, pp. 471–84.
46. G. Baril, C. Blanc, and N. Pébère: *J. Electrochem. Soc.*, 2001, vol. 148, pp. 469–96.
47. J.R. Galvele, R.M. Torresi, and R.M. Carranza: *Corros. Sci.*, 1990, vol. 31, pp. 563–71.
48. A. Gebert, U. Wolff, A. John, J. Eckert, and L. Schultz: *Mater. Sci. Eng. A*, 2001, vol. 299, pp. 125–35.
49. S.P. Harrington and T.M. Devine: *J. Electrochem. Soc.*, 2009, vol. 156, pp. 154–59.
50. P. Stefanov, D. Stoychev, M. Stoycheva, and T.S. Marinova: *Mater. Chem. Phys.*, 2000, vol. 65, pp. 212–15.
51. H.H. Huang: *Biomaterials*, 2003, vol. 24, pp. 1575–82.
52. G. Barral, S. Maximovitch, and F. Njanjo-Eyoke: *Electrochim. Acta*, 1996, vol. 41, pp. 1305–11.
53. J.M. Song, Y.S. Zou, C.C. Kuo, and S.C. Lin: *Corros. Sci.*, 2013, vol. 74, pp. 223–31.